RSC Advances

PAPER

View Article Online
View Journal | View Issue

Cite this: *RSC Adv.*, 2021, **11**, 3792

The roles of fused-ring organic semiconductor treatment on SnO_2 in enhancing perovskite solar cell performance†

Lu Ren, [abd] Lusheng Liang,[ad] Zhuangzhuang Zhang,[d] Zilong Zhang,[ad] Qiu Xiong,[abd] Nan Zhao,[c] Yaming Yu,[c] Rosario Scopelliti [e] and Peng Gao *[abd]

It took only 11 years for the power conversion efficiency (PCE) of perovskite solar cells (PSCs) to increase from 3.8% to 25.2%. It is worth noting that, as a new thin-film solar cell technique, defect passivation at the interface is crucial for the PSCs. Decorating and passivating the interface between the perovskite and electron transport layer (ETL) is an effective way to suppress the recombination of carriers at the interface and improve the PCE of the device. In this work, several acceptor–donor–acceptor (A–D–A) type fused-ring organic semiconductors (FROS) with indacenodithiophene (IDT) or indacenodithienothiophene (IDDT) as the bridging donor moiety and 1,3-diethyl-2-thiobarbituric or 1,1-dicyromethylene-3-indanone as the strong electron-withdrawing units, were deposited on the SnO_2 ETL to prepare efficient planar junction PSCs. The PCEs of the PSCs increased from 18.63% for the control device to 19.37%, 19.75%, and 19.32% after modification at the interface by three FROSs. Furthermore, impedance spectroscopy, steady-state and time-resolved photoluminescence spectra elucidated that the interface decorated by FROSs enhance not only the extraction of electrons but also the charge transportation at the interface between the perovskite and ETL. These results can provide significant insights in improving the perovskite/ETL interface and the photovoltaic performance of PSCs.

Received 6th January 2021
Accepted 8th January 2021

DOI: 10.1039/d1ra00090j

rsc.li/rsc-advances

Introduction

Organic-inorganic hybrid perovskite materials show excellent photoelectric properties (such as tunable bandgap, long carrier lifetime/diffusion length, low exciton binding energy, high extinction coefficient, high defect-tolerance, and solution processability). They are widely used in various optoelectronic devices, especially the perovskite solar cells (PSCs).[1–10]

The device structure of PSCs usually consists of transparent conductive oxides (*i.e.*, fluorine-doped tin oxide FTO and indium tin oxide ITO), electron transport layer (ETL, *e.g.*, TiO_2, SnO_2, ZnO, C_{60}), ABX_3 type perovskite layer (where the A is a cation, *e.g.*, methylammonium (MA^+), formamidinium (FA^+), Cs^+; B is a metal cation, *e.g.*, Pb^{2+}, Sn^{2+}; and X is an anion, *e.g.*, I^-, Br^-, Cl^-, SCN^-),[11] hole transport layer (HTL, *e.g.*, Spiro-MeOTAD, PTAA, P3HT, CuSCN, CuPc) and metal electrode (*e.g.*, Au, Ag).[3,12] The primary function of ETL is to transport electrons while blocking holes from recombination, which is essential for the PCE and lifespan properties of PSCs.[13] Due to the need for the high temperature (≥450 °C) annealing process, the application of traditional TiO_2 as ETL in energy-efficient PSCs is becoming unfavorable.[14,15] On the other hand, low temperature processable (<150 °C) SnO_2 with better optical and electric properties than TiO_2 is conceptually considered as a superior candidate for highly efficient PSCs.[16,17] So far, ETLs based on SnO_2 have demonstrated excellent features like high electron mobility, wide band gap,[18] good photostability and high transparency,[19] and good energy level alignment with the perovskite absorber.[20] However, it is worth noting that the defects at the SnO_2/perovskite interface vary dramatically depending on the fabrication methods, which will affect the performance and stability of the devices.[11,21,22] For example, these defects may cause charge accumulation and non-radiative recombination,[3] which will lead to the hysteresis effect, performance loss, and deterioration of device stability.[11,23] Researches have indicated that passivation at the SnO_2/perovskite interface can significantly inhibit the formation of

[a]*CAS Key Laboratory of Design and Assembly of Functional Nanostructures, Fujian Provincial Key Laboratory of Nanomaterials, Fujian Institute of Research on the Structure of Matter, Chinese Academy of Sciences, Fuzhou, Fujian 350002, China. E-mail: peng.gao@fjirsm.ac.cn*

[b]*University of Chinese Academy of Science, Beijing 100049, China*

[c]*College of Materials Science and Engineering, Huaqiao University, 361021 Xiamen, China*

[d]*Laboratory for Advanced Functional Materials, Xiamen Institute of Rare Earth Materials, Haixi Institute, Chinese Academy of Sciences, Xiamen 361021, China*

[e]*Institut des Sciences et Ingénierie Chimiques, Ecole Polytechnique Fédérale de Lausanne (EPFL), CH-1015 Lausanne, Switzerland*

† Electronic supplementary information (ESI) available: Fig. S1–S27 and Tables S1–S7 provide additional characterization including structure characterization, DFT calculation, thermal properties and device performance. CCDC 2036683 and 2036684. For ESI and crystallographic data in CIF or other electronic format see DOI: 10.1039/d1ra00090j

interface defects.[11,16] For example, fullerene derivatives,[13,14,24,25] graphene,[26] graphene quantum dots (GQDs),[27] methylammonium chloride,[28] fused-ring organic semiconductors (FROS),[29,30] ionic liquids,[22,31] and self-assembled monolayers[11] are used as passivators to promote the extraction of electrons from the perovskite layer to the ETLs.

The FROS materials have recently become popular non-fullerene acceptors in organic solar cells due to excellent characteristics such as tunable optical band gap and energy level, high electron mobility, excellent photo-thermal stability, *etc.*[32] Normally, such molecules are composed of a ring-fused backbone with two strong electron-withdrawing groups at both ends, which usually contain Lewis-base-type functional groups such as carbonyl groups, cyano groups, and thiocarbonyl groups. Therefore, the application of n-type FROS as a passivator at the interface between ETL and perovskite could effectively passivate the under-coordinated Pb^{2+} ions and further improve the performance of PSCs.

Herein, we use a series of n-type FROSs called IDT-T, IDT-I, and IDDT-T to passivate the interface between the perovskite layer and SnO_2 layer in PSCs, leading to reduced interfacial loss and less hysteresis in hopes of enhancing the performance of PSC devices. Among them, IDT-T and IDT-I are comprised of one IDT backbone and two 1,3-diethyl-2-thiobarbituric and two 1,1-dicyromethylene-3-indanone electron-withdrawing end groups, respectively. In comparison, IDDT-T is composed of an IDDT ore and two 1,3-diethyl-2-thiobarbituric terminal groups.[33–35] In the device structure of FTO/SnO_2/FROS/perovskite/Spiro-OMeTAD/Au, the effect of the three FROSs on the structure, morphology, and photoelectric properties of the interface are characterized and compared by scanning electron microscopy (SEM), steady-state/time-resolved photoluminescence spectroscopy, electrochemical impedance spectroscopy (EIS), and other techniques. The results of the work showed that the PCE of PSCs modified by the FROSs layer increased from 18.63% without interface modification to 19.37% (IDT-T), 19.75% (IDT-I), 19.32% (IDDT-T). This improvement is due to the larger grain size of the perovskite, shorter decay lifetimes, smaller series resistance, and larger recombination resistance of the device compared to undoped PSCs. The performances (V_{OC}, J_{SC}, and FF) of the PSCs modified by the FROS layer have been improved, but the efficiency does not increase significantly, which may be due to the matching degree between energy levels.

Results and discussion

The structure of the device and FROS molecules are shown in Fig. 1(a) and (b). Through density functional theory (DFT) calculations, we simulated the electron density distribution of three FROSs through the electrostatic potential surface (ESP) (Fig. 1(c)). High electron density regions are prominently present on electron-withdrawing groups, including carbonyl, thiocarbonyl, and dicyano groups. These groups can interact with insufficiently coordinated Pb^{2+} cations to passivate perovskite defects. The synthesis of IDT-T, IDT-I, and IDDT-T are shown in Section 1.3 in the ESI,† and IDDT-T is the first time compound synthesized. The structures of target FROSs are confirmed by ^{1}H-NMR (Fig. S4, S6, and S10†), ^{13}C-NMR (Fig. S11–S13†), MALDI-TOF MS spectroscopy (Fig. S14–S16†), and elemental analysis (Table S1†). Fourier transform infrared (FTIR) spectroscopy showed that the stretching vibration of the

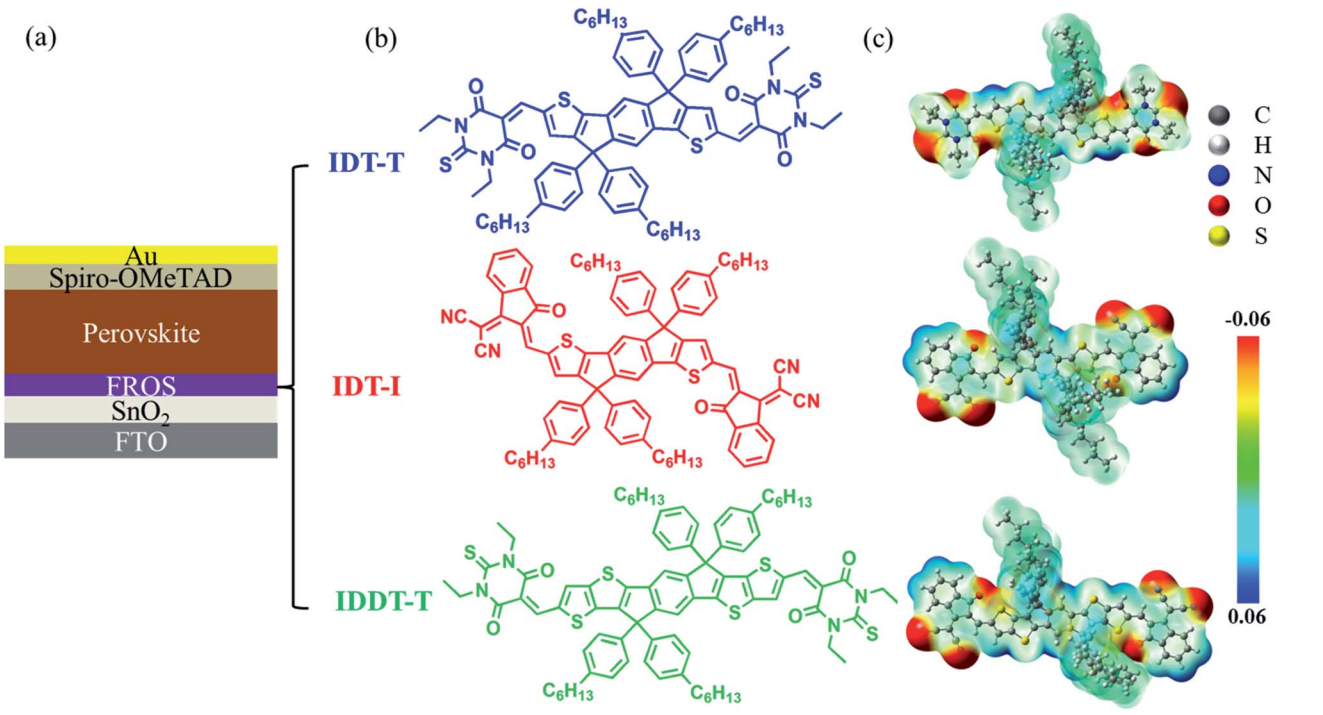

Fig. 1 (a) Device structure. (b) Chemical structures of IDT-T, IDT-I, and IDDT-T. (c) Calculated ESP profiles of IDT-T, IDT-I and IDDT-T.

carbonyl groups in the three FROSs appeared at 1630–1710 cm^{-1}. Among them, IDT-T and IDDT-T with thiocarbonyl groups showed a characteristic absorption peak at 1099 cm^{-1} (Fig. S17†), while the dicyano group in IDT-I showed its stretching vibration at 2218 cm^{-1}.

In order to accurately analyze the effect of different acceptor moiety on the molecular configuration and packing in the condensed state, single-crystal X-ray diffraction (SC-XRD) analysis was performed, and single crystals of IDT-T and IDT-I were successfully prepared by slowly diffusing methanol into their solutions in dichloromethane.[36] Fig. S18† shows the single-crystal structures of the two molecules observed from two perspectives. The corresponding crystallographic parameters are summarized in Table S2.† It can be seen from Fig. 2 that in a unit cell, two independent IDT-T molecules stack tightly *via* four O–H hydrogen bonds (symmetry, 2.717 Å and 2.613 Å) and two C–H–π (symmetry, 2.364 Å) noncovalent intermolecular short contacts (Fig. 2(a)). In the case of IDT-I, two independent molecules pack closely by C–H – C–H (2.297 Å) interactions (Fig. 2(c)).[37] Notably, both IDT-T and IDT-I exhibit intramolecular S···O=C short contacts with distances (2.648 Å and 2.620 Å) closer than the sum of the van der Waals radii of the S and O (3.25 Å), which can non-covalently lock the molecular conformation.[38–40] This interlocked network will not only provide better molecular coplanarity but also endow closed and ordered molecular packing.[36] The torsion angles between the bridging π backbones and the acceptors are 11.83° and 4.38° for IDT-T and IDT-I, respectively, indicating better planarity for IDT-I than IDT-T.

The thermal stability of the three FROSs was checked by thermogravimetric analysis (TGA) and differential scanning calorimetry (DSC). As shown in Fig. S20,† the thermal stability of IDT-I is higher than IDT-T and IDDT-T. At 5% weight loss, the decomposition temperatures (T_d) of IDT-T, IDT-I, and IDDT-T are 349 °C, 375 °C, and 342 °C, respectively. DSC measurement showed that the three FROSs did not show noticeable glass transition temperature (T_g) and melting temperature (T_m). This indicates that the three compounds are very stable within 300 °C without phase transition (Fig. S21†).

The ultraviolet-visible (UV-vis) absorption spectra of the FROSs show a similar profile (Fig. 3(a)) with two characteristic absorption peaks. The IDDT-T has a longer conjugation length than that of IDT-T, so the highest occupied molecular orbit (HOMO) energy level is more destabilized, and the absorption

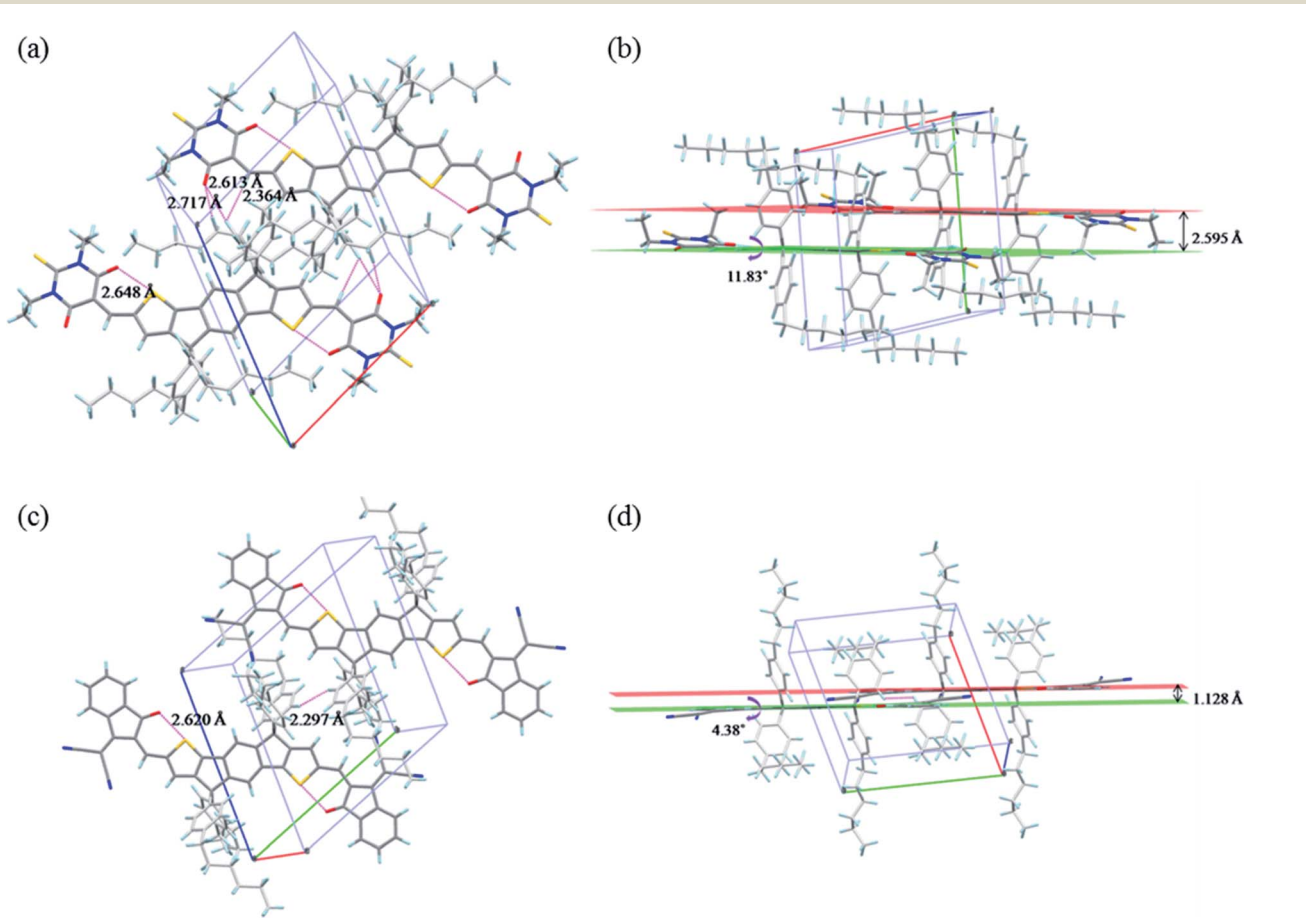

Fig. 2 The molecular stacking diagrams of (a and b) IDT-T and (c and d) IDT-I in a crystal cell from two perspectives. (a and c) Are front views; (b and d) are side views. Besides, the grey, light blue, dark blue, red, and yellow colored atoms represent C, H, N, O, and S atoms, respectively. The light grey atom is the C atom of the side chain (*p*-hexylbenzene). Noncovalent intermolecular short contacts of IDT-T and IDT-I were marked with magenta dash lines. The red and green planes are the planes of adjacent main chains.

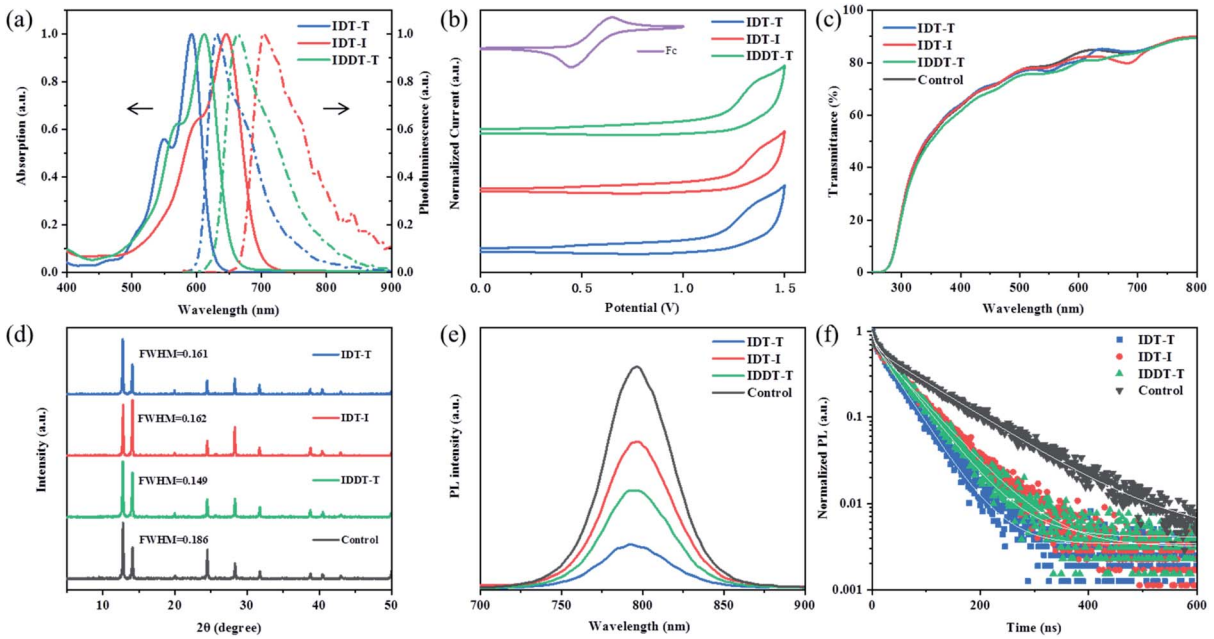

Fig. 3 (a) UV-Vis absorption spectra and fluorescence emission of three FROSs in CH_2Cl_2 solution. (b) Cyclic voltammetry of FROSs recorded in $CHCl_3$ containing 0.1 M $TBAPF_6$ as electrolyte at a scan rate of 100 mV s^{-1} with the ferrocene/ferrocenium redox couple (Fc/Fc^+) as the internal reference. (c) Transmittance spectroscopy of SnO_2 and SnO_2/FROS films prepared on FTO substrates (d) Thin-film XRD patterns of perovskites deposited on SnO_2 and SnO_2/FROS substrates, FWHM of these corresponding perovskite peaks at 14.1° were calculated and listed. (e) Steady-state PL spectra of pristine and three FROSs doped perovskite films. (f) Time-resolved photoluminescence of pristine and three FROSs doped perovskite films.

peak is slightly red-shifted. The introduction of the stronger electron-withdrawing dicyano groups stabilized the lowest unoccupied molecular orbital (LUMO) energy level further, thereby also reduces the bandgap of the system and shifts the absorption peak to a longer wavelength. Therefore, IDT-I showed the most red-shifted absorption band (646 nm) comparing to IDT-T (592 nm) and IDDT-T (612 nm). UV-Vis spectra of FROSs in thin-film state red-shifted 19 nm, 46 nm, and 20 nm for IDT-T, IDT-I, and IDDT-T, respectively, compared to those measured in dichloromethane (DCM), Fig. S22† suggesting intermolecular aggregation in the solid state.[34] Based on the intersection of the UV-vis spectra and fluorescence spectra (Fig. 3(a)), the optical bandgap (E_g^{opt}) of IDT-T, IDT-I, and IDDT-T are calculated as 2.03 eV, 1.83 eV, and 1.95 eV, respectively.

Besides, as shown in the cyclic voltammetry (CV) measurement in Fig. 3(b), all the three FROSs show irreversible oxidation potentials. Based on the onset of the CV curves, we can calculate the corresponding HOMO energy levels as −5.78 eV (IDT-T), −5.76 eV (IDT-I), and −5.69 eV (IDDT-T). The LUMO

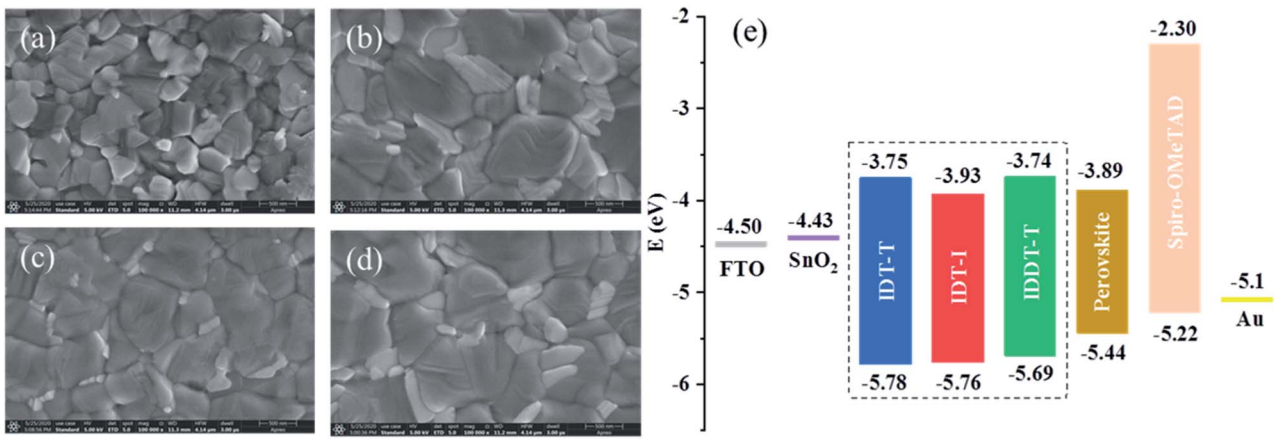

Fig. 4 SEM top-view images of (a) the pristine perovskite film and the perovskite films with (b) IDT-T, (c) IDT-I, and (d) IDDT-T optimized treatment conditions. (e) Energy-level diagrams of the corresponding materials of the device.[13,45]

Table 1 Electrochemical and DFT analysis of the FROSs

	λ_{onset} [nm]	E_g[a] [eV]	E_{HOMO}[b] [eV]	E_{LUMO}[c] [eV]	E_g^{cal} [eV]	E_{HOMO}^{cal} [eV]	E_{LUMO}^{cal} [eV]
IDT-T	612.8	2.03	−5.78	−3.75	2.44	−5.69	−3.25
IDT-I	679.8	1.83	−5.76	−3.93	2.24	−5.63	−3.39
IDDT-T	638.8	1.95	−5.69	−3.74	2.32	−5.45	−3.13

[a] $E_g = 1243/\lambda_{onset}$ (eV). [b] $E_{HOMO} = -5.1 - (E_{ox} - E_{1/2}(Fc/Fc^+))$ (eV). [c] $E_{LUMO} = E_g + E_{HOMO}$ (eV).

energy levels can then be subsequently calculated as −3.75 eV (IDT-T), −3.93 eV (IDT-I), and −3.74 eV (IDDT-T). As shown in the energy diagram in Fig. 4(e), the IDT-I has the best matched LUMO energy level with the conduction band of perovskite, favoring the transfer of electrons from the perovskite layer to the ETL. Moreover, DFT calculations are also used to estimate the HOMO and LUMO orbitals of FROSs. As shown in Table 1, a similar trend with the experimental values was achieved.

Fig. 3(c) shows the transmittance spectra of SnO_2 and SnO_2/FROS thin films prepared on FTO substrates. Compared with the SnO_2 substrate, the light transmittance of SnO_2/FROS reduced slightly for IDT-T at 470–630 nm, IDT-I at 470–735 nm, and IDDT-T at 300–800 nm. This indicates that incorporating the FROS interlayer does not induce significant optical losses.[41] The electron mobility of different FROSs based SnO_2 ETLs were measured using the space charge limited current (SCLC) model.[19] The result indicates that the introduction of ultrathin FROSs does not affect electron mobility significantly (Fig. S23 and Table S3†). To check the influence of the FROS layer on the perovskite layer deposited atop, thin-film X-ray diffraction (XRD) was used to characterize the solid structure of the perovskite films, and the results are displayed in Fig. 3(d). The diffraction peaks at 14.1°, 28.3°, and 31.8°, are attributed to the ⟨110⟩, ⟨220⟩, and ⟨310⟩ facets of the perovskite.[41–43] The peak at 12.7° results from excessive PbI_2, the existence of which has been demonstrated to have a positive effect on grain boundary passivation.[11,44] ⟨220⟩ crystal planes of FROSs compared to this from the pristine perovskite is a clear evidence of enhanced perovskite crystallinity. Generally, the addition of FROSs did not destroy the intragranular crystal structure of the perovskite. However, compared to the XRD of pristine perovskite film, the ⟨110⟩ reflection in the XRD of the perovskite films deposited on FROS modified SnO_2 is more intense with a smaller full-width at half-maximum (FWHM). This observation agrees with the enlarged grains shown by scanning electron microscope (SEM) in Fig. 4(a–d) and S24,† confirming the enhanced crystallinity in the presence of the FROS layer (*vide infra*).

To study the morphology of the perovskite films based on IDT-T, IDT-I, and IDDT-T, SEM top-view images of the pristine perovskite film and the perovskite films deposited on the FROS layer under optimized conditions are shown in Fig. 4. The comparison shows that the crystal grain size of the modified perovskite is significantly larger than that of the pristine perovskite, meaning the FROSs underlayer can help to promote the growth of perovskite crystal grains. The reason behind the increased grain size after FROS modification is linked with the hydrophobic nature of organic FROSs surface, which affects the nucleation and grain growth behavior.[46] Larger grains can reduce the defects of the perovskite and hence the interfacial recombination of the photo-generated charges.[47] Besides, the cross-sectional SEM of SnO_2/FROS-based PSCs (Fig. S24†) shows that the perovskite crystal grains penetrate almost the entire perovskite light-absorbing layer in the longitudinal direction. In contrast, the perovskite on pristine SnO_2 shows more grain boundaries, which may be responsible for the higher interfacial recombination. XRD and SEM demonstrated that the addition of the FROS layer enhances the crystallization of perovskite.

Device performances are closely correlated to charge dynamics in perovskite solar cells. The electronic quality and charge transfer at the ETL/perovskite interface was evaluated by steady-state photoluminescence (PL) and time-resolved photoluminescence (TRPL) measurements.[48–50] Fig. 3(e) represents the steady-state PL spectra of the perovskite films deposited on neat SnO_2 and SnO_2/FROSs, respectively. Significant PL quenching is observed on perovskite films deposited on SnO_2/FROS, contrasting to the intensive emission peak of the reference sample at ∼795 nm. This could be caused by the improved charge carrier extraction after the insertion of the FROS and reduced surface charge trapping. The FROS films could facilitate the charge transport between perovskite and ETL.

To further study the effect of the FROS layer on the dissociation and recombination of the charge carriers, TRPL was conducted. Fig. 3(f) exhibits the TRPL spectra of SnO_2/perovskite film and the perovskite films deposited on SnO_2/FROS. The PL decay curves were fitted by a biexponential decay function, including a fast decay (τ_1) and a slow decay (τ_2) component.[13,51] τ_1 can be attributed to the PL quenching *via* trap states or ETL/perovskite interfacial charge transfer,[52,53] and τ_2 can be attributed to the PL quenching by the radiative recombination of free charges.[44,54] The detailed fitting parameters are listed in Table S4.† The average lifetimes (τ_{avg}) of different films were estimated as 105.39, 44.10, 61.02, and 53.03 ns for the SnO_2/perovskite, SnO_2/IDT-T/perovskite, SnO_2/IDT-I/perovskite, and SnO_2/IDDT-T/perovskite, respectively. The decay lifetimes of SnO_2/FROS/perovskite decreased dramatically compared to that of the SnO_2/perovskite. After using the FROS modified SnO_2, the electrons can transfer more efficiently from the perovskite active layer to the ETL, and less recombination occurred inside the perovskite layer. The TRPL result is consistent with the steady PL measurement.

In Fig. 5(a), the current density–voltage (J–V) characteristics of the champion devices based on SnO_2 and SnO_2/FROS

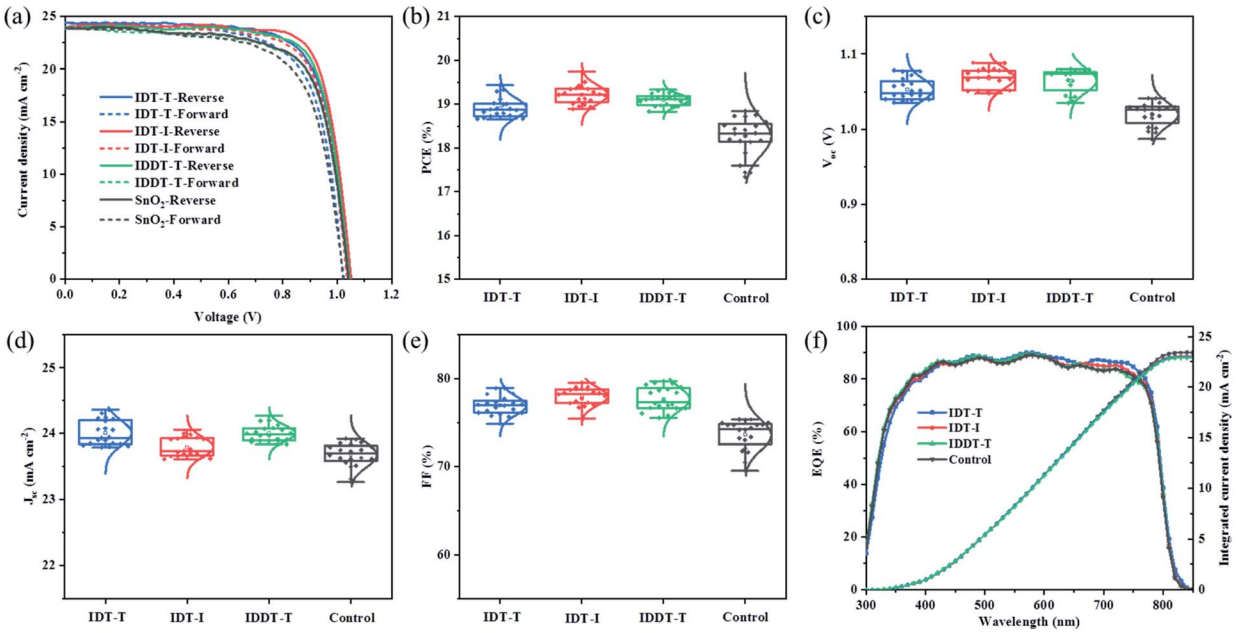

Fig. 5 (a) J–V curves of the best-performance devices with SnO_2 and SnO_2/FROS substrates by forward and reverse scan. (b–e) Statistics of PCE, V_{OC}, J_{SC}, and FF of devices with SnO_2 and SnO_2/FROS substrates (20 devices for each condition). (f) The external quantum efficiency (EQE) spectra and the corresponding integrated J_{SC} of the best-performance devices with SnO_2 and SnO_2/FROS substrates.

substrates were measured under simulated air mass 1.5 global (AM 1.5G) solar irradiation. The corresponding detailed photovoltaic parameters of devices based on pristine SnO_2 and SnO_2/FROS substrates are summarized in Table 2. The most important observation from the J–V curves was the beneficial role of the FROS decoration of the SnO_2 film. The best PCEs from SnO_2/FROS based device (SnO_2/IDT-T: 19.37%, SnO_2/IDT-I: 19.75%, SnO_2/IDDT-T: 19.32%) are all enhanced comparing to the neat SnO_2 based device (18.63%) in the reverse scanning (RS) direction. To quantify the hysteresis effect, the hysteresis index (HI) was calculated according to the method described in the previous reports.[55,56] Compared with SnO_2 based device (HI = 7.19%), SnO_2/IDT-I based device has lower HI (4.4%), while SnO_2/IDT-T and SnO_2/IDDT-T based devices show slightly increased HI (9.98% and 7.61%). The effective suppression of hysteresis by the IDT-I treatment leads to optimized efficiency and significantly improved consistency in the extracted photovoltaic parameters under different scan directions.[41]

Fig. 5(b) shows the statistics of PCE of devices with SnO_2 and SnO_2/FROS substrates. The average PCEs of the devices with SnO_2, SnO_2/IDT-T, SnO_2/IDT-I, and SnO_2/IDDT-T ETLs are 18.27%, 18.92%, 19.22%, and 19.10%, respectively. The corresponding statistic values of V_{OC}, J_{SC}, and FF are listed in Fig. 5(c–e), respectively (Table S5†). Devices based on SnO_2/IDT-I ETL has the highest PCE due to the outstanding V_{OC} and FF, which can be attributed to the following reasons: (i) the dicyano group of IDT-I passivates the defect of perovskite film and thereby reduces the interface carrier recombination;[57] (ii) the more favorable LUMO level of IDT-I (Fig. 4(e)) benefits the electrons transport from the perovskite layer to the SnO_2.

Besides, the EQE spectra and integrated J_{SC} of the best-performance devices with SnO_2 and SnO_2/FROS substrates are shown in Fig. 5(f). The devices with the SnO_2/FROS ETL

Table 2 Photovoltaic parameters for the best-performing devices with SnO_2 and SnO_2/FROS substrates

Material	Sweep	V_{OC} (V)	J_{SC} (mA cm^{-2})	FF (%)	Efficiency (%)	HI[a] (%)
SnO_2	RS	1.029	23.61	76.70	18.63	7.19
	FS	1.021	23.46	72.19	17.29	
SnO_2/IDT-T	RS	1.023	24.00	78.91	19.37	9.71
	FS	1.021	24.40	70.16	17.49	
SnO_2/IDT-I	RS	1.051	24.02	78.22	19.75	4.40
	FS	1.080	23.68	73.82	18.88	
SnO_2/IDDT-T	RS	1.022	23.80	79.44	19.32	7.61
	FS	1.055	23.25	72.77	17.85	

[a] HI = (PCERS − PCEFS)/PCERS % 100%

represented higher quantum efficiency in the range of 300–850 nm than the devices with the SnO_2 substrate. The integrated photocurrent values from the EQE spectra of the devices with SnO_2, SnO_2/IDT-T, SnO_2/IDT-I, and SnO_2/IDDT-T substrates are 22.90, 23.44, 23.07, and 23.03 mA cm^{-2}. The deviations of the corresponding samples are 3.01%, 2.66%, 3.96%, and 3.24%, respectively, which are within 4% error compared to the corresponding J_{SC} obtained from *J–V* curves.

The EIS measurement of the devices was conducted to analyze the effect of the FROS layer on the interfacial charge transfer and carrier recombination behavior. Fig. 6(a) depicts the Nyquist plots of the devices with and without the FROS layer and equivalent circuits (inset). The fitted parameters by the equivalent circuits are listed in Table S7.† In the Nyquist plots, there are two different semicircles locates at different frequency ranges. The high-frequency region and low-frequency region correspond to the charge transfer resistance (R_{ct}) and recombination resistance (R_{rec}), respectively.[58,59] It notes that the series resistance in the PSC could be reduced through the introduction of FROS. The R_s of the optimized FROS containing devices are almost half of the R_s of the reference device, indicating reduced contact resistance at the perovskite/ETL interface. Although the R_{ct}s of the optimized devices are slightly higher than that of the reference device, their R_{rec}s are significantly increased. A higher R_{rec} suggests reduced non-radiative recombination, so the FROS treated devices all show higher V_{OC}s than that of the reference device, which may be attributed to the increased grain size of perovskite as discussed above (Fig. 4(a–d) and S24†). Therefore, these results also revealed that, after introducing the FROS layer, the carrier transport efficiency is improved and the carrier recombination is suppressed, both of which are beneficial for increasing FF value (Fig. 5(e)).[60,61]

To further study the effect of FROS passivation on perovskite defect, the SCLC measurement based on electronic-only devices (FTO/SnO_2/FROS/perovskite/PCBM/Ag) with or without FROS was conducted to obtain the trap density statistics of perovskite films.[62,63] The average trap densities were determined from the dark current–voltage characteristics (electronic-only, Fig. S25†) based on eqn (S2), ESI.† The results show that after introducing the FROS, the trap density decreases from 1.19×10^{15} cm^{-3} for control to 9.82×10^{14} cm^{-3}, 8.16×10^{14} cm^{-3} and 8.80×10^{14} cm^{-3} for SnO_2/IDT-T, SnO_2/IDT-I, and SnO_2/IDDT-T samples, respectively. The reduced trap density indicates that FROS materials could passivate the defects such as under-coordinated Pb^{2+} ions using their Lewis base type functional groups like carbonyl, cyano, and thiocarbonyl groups.

The stability is also crucial to the development of PSCs. Fig. S26† displays the long-term humidity stability of different ETL-based devices. The sample SnO_2/IDT-I showed slightly better stability than other samples under 10–20% RH in the atmosphere after 240 h, even though the performance of all samples did not exhibit an apparent deterioration. Fig. 6(b) shows the steady-state power output and photocurrent output of the best devices, measured at its maximum power point (V_{MPP} = 0.87 V) for 300 s. The device with SnO_2 substrate exhibits a photocurrent of 20.7 mA cm^{-2} and a PCE of 18.0%. In comparison, the device with SnO_2/IDT-T, SnO_2/IDT-I, and SnO_2/IDDT-T substrate exhibit photocurrents of 21.9 mA cm^{-2}, 22.2 mA cm^{-2}, and 21.7 mA cm^{-2} as well as PCEs of 19.1%, 19.3%, and 18.8%, respectively. Compared with the values extracted from the *J–V* curves (PCE_{J-V}), the steady-state PCEs (PCE_{SS}) of the four device structures lose 3.3%, 1.6%, 2.3%, and 2.5% ((PCE_{J-V}–PCE_{SS})/PCE_{J-V} × 100%) for the control, SnO_2/IDT-T, SnO_2/IDT-I and SnO_2/IDDT-T samples, respectively. It indicates that the devices with SnO_2/FROS substrate have lower PCE loss and better power output stability than control. This improvement could be ascribed to the reduced defect in the devices. Firstly, the incorporation of FROS between SnO_2 and perovskite can passivate the defect at the SnO_2/perovskite interface through the interaction between the Lewis-base-groups with under-coordinated Pb^{2+} ions in perovskite. Secondly, the

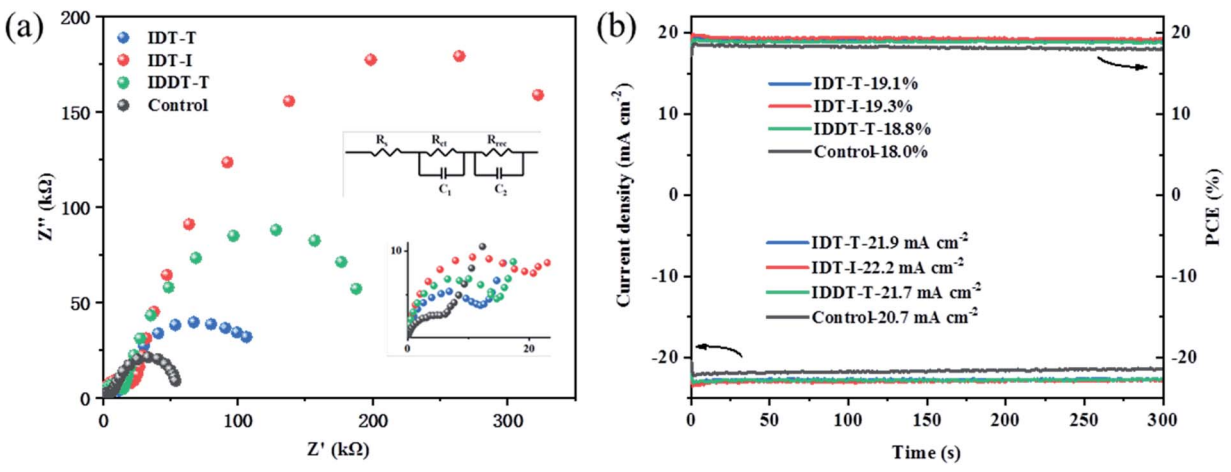

Fig. 6 (a) Electrical impedance spectroscopy (EIS), Nyquist plots of the devices with SnO_2, SnO_2/IDT-T, SnO_2/IDT-I, and SnO_2/IDDT-T substrates at −0.5 V under dark conditions, respectively (equivalent circuit model for the Nyquist plots.[53] R_s: series resistance. R_{ct}: charge transfer resistance. R_{rec}: resistance of interfacial recombination. *C*: capacitance). (b) Maximum power output and current density of the device with SnO_2, SnO_2/IDT-T, SnO_2/IDT-I, and SnO_2/IDDT-T substrates (at 0.87 V).

introduction of FROS improved the morphology of perovskites with enlarged grains, thereby reducing the grain boundaries and the defects therein. One of the SnO_2/IDT-I based devices could keep 97.4% of initial PCE after 2400 s measurement at its maximum power point (Fig. S27†). These results prove that the addition of the FROS layer improves device stability.

Conclusions

In this paper, three FROS materials are used as the interface modification layer at the ETL/perovskite layer interface to improve the PCEs of PSCs significantly. With the insertion of the FROS layer, PSCs demonstrated superior properties to the control device based on only the SnO_2 substrate. The results show that the interface modification by FROSs improves the morphology of the perovskite film, promotes the high-quality growth of perovskite grains, dramatically reduces the charge recombination at the surface and the interface, and significantly improves the extraction rate and transport efficiency of photo-generated carriers. Consequently, FROS modification is a simple and effective interface optimization method for preparing efficient and stable PSCs. Notable, among them, IDT-I with higher decomposition temperature, narrower optical bandgap, and the highest average V_{OC} (1.068 V), FF (77.99%), PCE (19.75%), showed the lowest HI (4.4%). The good stability of the three FROSs has essential practical application value and academic significance for improving the photovoltaic performance of PSCs.

Conflicts of interest

There are no conflicts to declare.

Acknowledgements

P. G. acknowledges the financial support from the National Natural Science Foundation of China (Grant No. 21975260) and the Recruitment Program of Global Experts of China (No. 201613, Y8d3071caa). We thank Prof. Yuanzhi Tan from Xiamen University for the measurement of MALDI-TOF data and Yaming Yu from Huaqiao University for the measurement of DSC data.

Notes and references

1 P. Gao, M. Grätzel and M. K. Nazeeruddin, *Energy Environ. Sci.*, 2014, **7**, 2448–2463.
2 A. R. Bin Mohd Yusoff, P. Gao and M. K. Nazeeruddin, *Coord. Chem. Rev.*, 2018, **373**, 258–294.
3 J. Chen and N. G. Park, *ACS Energy Lett.*, 2020, **5**, 2742–2786.
4 N. J. Jeon, J. H. Noh, W. S. Yang, Y. C. Kim, S. Ryu, J. Seo and S. Il Seok, *Nature*, 2015, **517**, 476–480.
5 A. Al-Ashouri, E. Köhnen, B. Li, A. Magomedov, H. Hempel, P. Caprioglio, J. A. Márquez, A. B. Morales Vilches, E. Kasparavicius, J. A. Smith, N. Phung, D. Menzel, M. Grischek, L. Kegelmann, D. Skroblin, C. Gollwitzer, T. Malinauskas, M. Jošt, G. Matič, B. Rech, R. Schlatmann, M. Topič, L. Korte, A. Abate, B. Stannowski, D. Neher, M. Stolterfoht, T. Unold, V. Getautis and S. Albrecht, *Science*, 2020, **370**, 1300–1309.
6 L. Liang and P. Gao, *Adv. Sci.*, 2018, **5**, 1700331.
7 M. Wang, H. Wang, W. Li, X. Hu, K. Sun and Z. Zang, *J. Mater. Chem. A*, 2019, **7**, 26421–26428.
8 B. Zhao, S. Bai, V. Kim, R. Lamboll, R. Shivanna, F. Auras, J. M. Richter, L. Yang, L. Dai, M. Alsari, X.-J. J. She, L. Liang, J. Zhang, S. Lilliu, P. Gao, H. J. Snaith, J. Wang, N. C. Greenham, R. H. Friend and D. Di, *Nat. Photonics*, 2018, **12**, 783–789.
9 L. Liang, Y. Cai, X. Li, M. K. Nazeeruddin and P. Gao, *Nano Energy*, 2018, **52**, 211–238.
10 Z. Zhang, Z. Li, L. Meng, S. Lien and P. Gao, *Adv. Funct. Mater.*, 2020, **30**, 2001904.
11 L. Zuo, Q. Chen, N. De Marco, Y. T. Hsieh, H. Chen, P. Sun, S. Y. Chang, H. Zhao, S. Dong and Y. Yang, *Nano Lett.*, 2017, **17**, 269–275.
12 Z. Zhao, W. Sun, Y. Li, S. Ye, H. Rao, F. Gu, Z. Liu, Z. Bian and C. Huang, *J. Mater. Chem. A*, 2017, **5**, 4756–4773.
13 T. Cao, K. Chen, Q. Chen, Y. Zhou, N. Chen and Y. Li, *ACS Appl. Mater. Interfaces*, 2019, **11**, 33825–33834.
14 J. Wang, K. Datta, C. H. L. Weijtens, M. M. Wienk and R. A. J. Janssen, *Adv. Funct. Mater.*, 2019, **29**, 1905883.
15 H. Kim, K. G. Lim and T. W. Lee, *Energy Environ. Sci.*, 2016, **9**, 12–30.
16 L. Xiong, Y. Guo, J. Wen, H. Liu, G. Yang, P. Qin and G. Fang, *Adv. Funct. Mater.*, 2018, **28**, 1–18.
17 Q. Xiong, L. Yang, Q. Zhou, T. Wu, C. Mai, Z. Wang, S. Wu, X. Li and P. Gao, *ACS Appl. Mater. Interfaces*, 2020, **12**, 46306–46316.
18 W. Ke, G. Fang, Q. Liu, L. Xiong, P. Qin, H. Tao, J. Wang, H. Lei, B. Li, J. Wan, G. Yang and Y. Yan, *J. Am. Chem. Soc.*, 2015, **137**, 6730–6733.
19 Q. Jiang, L. Zhang, H. Wang, X. Yang, J. Meng, H. Liu, Z. Yin, J. Wu, X. Zhang and J. You, *Nat. Energy*, 2017, **2**, 16177.
20 J. P. Correa Baena, L. Steier, W. Tress, M. Saliba, S. Neutzner, T. Matsui, F. Giordano, T. J. Jacobsson, A. R. Srimath Kandada, S. M. Zakeeruddin, A. Petrozza, A. Abate, M. K. Nazeeruddin, M. Grätzel and A. Hagfeldt, *Energy Environ. Sci.*, 2015, **8**, 2928–2934.
21 Q. Jiang, X. Zhang and J. You, *Small*, 2018, **14**, 1–14.
22 K. Choi, J. Lee, H. Il Kim, C. W. Park, G. W. Kim, H. Choi, S. Park, S. A. Park and T. Park, *Energy Environ. Sci.*, 2018, **11**, 3238–3247.
23 S. A. L. L. Weber, I. M. Hermes, S.-H. Turren-Cruz, C. Gort, V. W. Bergmann, L. Gilson, A. Hagfeldt, M. Graetzel, W. Tress and R. Berger, *Energy Environ. Sci.*, 2018, **11**, 2404–2413.
24 A. Abrusci, S. D. Stranks, P. Docampo, H. L. Yip, A. K. Y. Jen and H. J. Snaith, *Nano Lett.*, 2013, **13**, 3124–3128.
25 X. Hu, H. Wang, M. Wang and Z. Zang, *Sol. Energy*, 2020, **206**, 816–825.
26 J. T. W. Wang, J. M. Ball, E. M. Barea, A. Abate, J. A. Alexander-Webber, J. Huang, M. Saliba, I. Mora-Sero, J. Bisquert, H. J. Snaith and R. J. Nicholas, *Nano Lett.*, 2014, **14**, 724–730.

27 D. Shen, W. Zhang, F. Xie, Y. Li, A. Abate and M. Wei, *J. Power Sources*, 2018, **402**, 320–326.
28 X. Hu, H. Wang, Y. Ying, M. Wang, C. Zhang, Y. Ding, H. Li, W. Li, S. Zhao and Z. Zang, *J. Power Sources*, 2020, **480**, 229073.
29 B. Du, D. Zhao, Z. Hou, L. Zheng, X. Liu, D. Chen, C. Gao and D. Yun, *Chin. Sci. Bull.*, 2019, **64**, 1887–1895.
30 J. Jiang, Z. Jin, J. Lei, Q. Wang, X. Zhang, J. Zhang, F. Gao and S. Liu, *J. Mater. Chem. A*, 2017, **5**, 9514–9522.
31 J. Chen, X. Zhao, S. Kim and N. Park, *Adv. Mater.*, 2019, 1902902.
32 Y. Lin, F. Zhao, Q. He, L. Huo, Y. Wu, T. C. Parker, W. Ma, Y. Sun, C. Wang, D. Zhu, A. J. Heeger, S. R. Marder and X. Zhan, *J. Am. Chem. Soc.*, 2016, **138**, 4955–4961.
33 Z. Zhang, X. Cui, M. Li, Y. Liu, D. Li, P. Jiang and Z. Bo, *RSC Adv.*, 2019, **9**, 39163–39169.
34 L. Xiao, B. He, Q. Hu, L. Maserati, Y. Zhao, B. Yang, M. A. Kolaczkowski, C. L. Anderson, N. J. Borys, L. M. Klivansky, T. L. Chen, A. M. Schwartzberg, T. P. Russell, Y. Cao, X. Peng and Y. Liu, *Joule*, 2018, **2**, 2154–2166.
35 B. Gao, H. Yao, B. Jang, J. Zhu, R. Yu, Y. Cui, F. Wang, J. Hou, H. Y. Woo and J. Hou, *J. Mater. Chem. A*, 2018, **6**, 2664–2670.
36 J. Qu, H. Chen, J. Zhou, H. Lai, T. Liu, P. Chao, D. Li, Z. Xie, F. He and Y. Ma, *ACS Appl. Mater. Interfaces*, 2018, **10**, 39992–40000.
37 J. Xu, L. Liang, C. Mai, Z. Zhang, Q. Zhou, Q. Xiong, Z. Zhang, L. Deng and P. Gao, *Nanoscale*, 2020, **12**, 13157–13164.
38 T. J. Aldrich, M. Matta, W. Zhu, S. M. Swick, C. L. Stern, G. C. Schatz, A. Facchetti, F. S. Melkonyan and T. J. Marks, *J. Am. Chem. Soc.*, 2019, **141**, 3274–3287.
39 N. E. Jackson, B. M. Savoie, K. L. Kohlstedt, M. Olvera De La Cruz, G. C. Schatz, L. X. Chen and M. A. Ratner, *J. Am. Chem. Soc.*, 2013, **135**, 10475–10483.
40 H. Huang, L. Yang, A. Facchetti and T. J. Marks, *Chem. Rev.*, 2017, **117**, 10291–10318.
41 S. You, H. Wang, S. Bi, J. Zhou, L. Qin, X. Qiu, Z. Zhao, Y. Xu, Y. Zhang, X. Shi, H. Zhou and Z. Tang, *Adv. Mater.*, 2018, **30**, 1706924.
42 Y. Q. Zhao, B. Liu, Z. L. Yu, J. M. Ma, Q. Wan, P. Bin He and M. Q. Cai, *J. Mater. Chem. C*, 2017, **5**, 5356–5364.
43 S. Bag, J. R. Deneault and M. F. Durstock, *Adv. Energy Mater.*, 2017, **7**, 1–11.
44 Q. Chen, H. Zhou, T.-B. Song, S. Luo, Z. Hong, H.-S. Duan, L. Dou, Y. Liu and Y. Yang, *Nano Lett.*, 2014, **14**, 4158–4163.
45 X. Zhao, C. Yao, T. Liu, J. C. Hamill, G. O. Ngongang Ndjawa, G. Cheng, N. Yao, H. Meng and Y. L. Loo, *Adv. Mater.*, 2019, **31**, 1–9.
46 C. Bi, Q. Wang, Y. Shao, Y. Yuan, Z. Xiao and J. Huang, *Nat. Commun.*, 2015, **6**, 7747.
47 M. Qin, J. Cao, T. Zhang, J. Mai, T. K. Lau, S. Zhou, Y. Zhou, J. Wang, Y. J. Hsu, N. Zhao, J. Xu, X. Zhan and X. Lu, *Adv. Energy Mater.*, 2018, **8**, 1–9.
48 D. Yang, T. Sano, Y. Yaguchi, H. Sun, H. Sasabe and J. Kido, *Adv. Funct. Mater.*, 2019, **29**, 1–6.
49 S. D. Stranks, G. E. Eperon, G. Grancini, C. Menelaou, M. J. P. P. Alcocer, T. Leijtens, L. M. Herz, A. Petrozza and H. J. Snaith, *Science*, 2013, **342**, 341–344.
50 D. Bi, W. Tress, M. I. Dar, P. Gao, J. Luo, C. Renevier, K. Schenk, A. Abate, F. Giordano, J.-P. Correa Baena, J. Decoppet, S. M. Zakeeruddin, M. K. Nazeeruddin, M. Grätzel and A. Hagfeldt, *Sci. Adv.*, 2016, **2**, e1501170.
51 T. Cao, P. Huang, K. Zhang, Z. Sun, K. Zhu, L. Yuan, K. Chen, N. Chen and Y. Li, *J. Mater. Chem. A*, 2018, **6**, 3435–3443.
52 J.-S. Yeo, R. Kang, S. Lee, Y.-J. Jeon, N. Myoung, C.-L. Lee, D.-Y. Kim, J.-M. Yun, Y.-H. Seo, S.-S. Kim and S.-I. Na, *Nano Energy*, 2015, **12**, 96–104.
53 W. Hu, W. Zhou, X. Lei, P. Zhou, M. Zhang, T. Chen, H. Zeng, J. Zhu, S. Dai, S. Yang and S. Yang, *Adv. Mater.*, 2019, **31**, 1–12.
54 O. Oni, K. Sujit, S. Kasemsuwan, T. Sakpuaram and D. U. Pfeiffer, *Vet. Rec.*, 2007, **160**, 368–371.
55 J. Cao, Y.-M. Liu, X. Jing, J. Yin, J. Li, B. Xu, Y.-Z. Tan and N. Zheng, *J. Am. Chem. Soc.*, 2015, **137**, 10914–10917.
56 S. You, S. Bi, J. Huang, Q. Jia, Y. Yuan, Y. Xia, Z. Xiao, Z. Sun, J. Liu, S. Sun and Z. Zhao, *Chem.–Eur. J.*, 2017, **23**, 18140–18145.
57 I. Gelmetti, N. F. Montcada, A. Pérez-Rodríguez, E. Barrena, C. Ocal, I. García-Benito, A. Molina-Ontoria, N. Martín, A. Vidal-Ferran and E. Palomares, *Energy Environ. Sci.*, 2019, **12**, 1309–1316.
58 T. Bu, J. Li, F. Zheng, W. Chen, X. Wen, Z. Ku, Y. Peng, J. Zhong, Y.-B. Cheng and F. Huang, *Nat. Commun.*, 2018, **9**, 4609.
59 X. Yin, J. Zhai, P. Du, N. Li, L. Song, J. Xiong and F. Ko, *ChemSusChem*, 2020, **13**, 1006–1012.
60 W. Zhou, P. Zhou, X. Lei, Z. Fang, M. Zhang, Q. Liu, T. Chen, H. Zeng, L. Ding, J. Zhu, S. Dai and S. Yang, *ACS Appl. Mater. Interfaces*, 2018, **10**, 1897–1908.
61 J. Song, E. Zheng, X. F. Wang, W. Tian and T. Miyasaka, *Sol. Energy Mater. Sol. Cells*, 2016, **144**, 623–630.
62 L. Liang, H. Luo, J. Hu, H. Li and P. Gao, *Adv. Energy Mater.*, 2020, **10**, 2000197.
63 T. Niu, J. Lu, M.-C. Tang, D. Barrit, D.-M. Smilgies, Z. Yang, J. Li, Y. Fan, T. Luo, I. McCulloch, A. Amassian, S. Liu and K. Zhao, *Energy Environ. Sci.*, 2018, **11**, 3358–3366.